Complex rupture and triggered aseismic creep during the August 14, 2021 Haiti earthquake from satellite geodesy

J. Maurer, R. Dutta, A. Vernon, and S. Vajedian

Missouri University of Science and Technology, Geological Sciences and Geological and Petroleum Engineering, Rolla, MO 65401, United States

Corresponding author: Jeremy Maurer (jmaurer@mst.edu)

Key Points:

- The 2021 Haiti earthquake ruptured the Enriquillo-Plantain Garden Fault as thrust slip east of Pic Macaya and left-lateral slip to the west
- Slip occurred on multiple fault segments and jumped across the restraining bend at Pic Macaya
- InSAR observations indicate afterslip in the four days following the event of a similar magnitude to the coseismic slip

Abstract

The 2021 August 14 M_W 7.2 Nippes, Haiti earthquake occurred 75 km west of the epicenter of the 2010 Leogane earthquake (Haiti) on the transpressive Caribbean - North America (CA-NA) plate boundary. We present an updated fault map for Hispaniola and model coseismic and early postseismic fault slip using Interferometric Synthetic Aperture RADAR (InSAR) and pixel offsets. We find the earthquake ruptured multiple segments of the Enriquillo-Plantain Garden Fault Zone (EPGFZ). Slip occurred in two main sub-events separated by 60 km on either side of a restraining bend at Pic Macaya, with ~2.7 m of peak reverse-slip east of the bend. To the west, slip jumps the restraining bend and further ruptures with ~1.3 meters of left-lateral slip. Afterslip in the four days following the event occurred at shallow depth and adjacent to the coseismic rupture areas and reached the surface to the east of Pic Macaya.

Plain Language Summary

On August 14, 2021, a large M_W7.2 earthquake struck southwestern Haiti, 75 km to the west of the 2010 Leogane, Haiti earthquake. We use remotely-sensed data from two SAR missions, ALOS-2 and Sentinel-1, and a new fault map database to study the earthquake and try to determine which faults slipped and where, and how much. We built a model of fault slip during the earthquake and aseismic slip that followed the earthquake, called afterslip. By comparing our results with previously published results using seismic data, we suggest that the earthquake started out with reverse slip on the Enriquillo-Plantain Garden Fault Zone (EPGFZ) near the hypocenter. It then jumped the restraining bend in the EPGFZ near Pic Macaya, and ruptured west of the restraining bend with left-lateral slip. The earthquake appears to be very complex and may have also ruptured some nearby faults. Afterslip in the four days following the earthquake was nearly as large as the earthquake, reaching the surface after ~3 days. Taken together, the modeling results paint a picture of a very complex fault system with highly variable stress and stability.

1 Introduction

The August 14, 2021 M_W7.2 Nippes earthquake struck the Tiburon peninsula in southwest Haiti and affected 800,000 people, caused over 2,000 deaths, and resulted in 1.6 billion USD in economic losses (UN-OCHA, 2021). The earthquake occurred just 11.5 years after the devastating M_w7.0 2010 earthquake that happened near Port-au-Prince, Haiti (**Figure 1**), and left a 75-km seismic gap between the two events. Haiti occupies the western third of the island of Hispaniola within the Gonave microplate on the boundary between the converging Caribbean (CA) and North American (NA) plates (Mann et al., 1995; Benford et al., 2012). Based on the USGS moment tensor solution (**Figure 1**), the Nippes earthquake was an oblique left-lateral thrust event that occurred on or near the Enriquillo-Plantain Garden Fault Zone (EPGFZ), a major plate-bounding strike-slip fault in the Tiburon peninsula (Supp. Fig. 1). The EPGFZ is a well-expressed major fault system that is thought to have ruptured in major historic earthquakes (e.g. Prentice, 2010; Bakun et al., 2012) and accommodates a large fraction of the 19 mm/yr N73E CA-NA relative plate motion (Mann et al., 2002; DeMets et al., 2010; Benford et al., 2012; Symithe et al., 2015; Calais et al., 2016). The EPGFZ is the eastward extension of the Walton fault east of Jamaica and may merge with the Muertos Trough offshore southern

Hispaniola (DeMets and Wiggins-Grandison, 2007; Leroy et al., 2015) or die out (Saint-Fleur et al., 2020). Faults on the Tiburon peninsula accommodate both strike-slip and compressional motion (Benford et al., 2012; Corbeau et al., 2016; Symithe and Calais, 2016), but the EPGFZ itself has been traditionally considered to be primarily a strike-slip fault with a dip near vertical (e.g., Mann et al., 1995; Prentice et al., 2010; Douilly et al., 2013; Symithe et al., 2013; Saint-Fleur et al., 2015).

Similar to the 2010 earthquake, the Nippes earthquake appears to be complex and involve both reverse- and left-lateral slip. Okuwaki and Fan (2022) used teleseismic finite-fault inversion and P-wave back-projection and found that the earthquake ruptured two separate regions of southwest Haiti, first near the event hypocenter with primarily reverse faulting, and the other west of the restraining bend at Pic Macaya (**Figure 1a**) with primarily left-lateral faulting. They argue that neither sub-event occurred on the EPGFZ but on different nearby faults. However, the dip-angle and geometry of the EPGFZ is not well known. The earthquake left a 75-km seismic gap between the location of the 2010 and 2021 events, with no large aftershocks in the gap region after either earthquake (**Figure 1a**). Instead, aftershocks of the 2010 earthquake followed a thrust fault offshore, while aftershocks of the 2021 earthquake were mostly within and near the mainshock location.

In this study, we analyze Synthetic Aperture Radar (SAR) data from Copernicus Sentinel-1 and Interferometric SAR (InSAR) images from Sentinel-1 and the Japan Aerospace Exploration Agency (JAXA) Advanced Land Observation Satellite-2 (ALOS-2) satellites (**Figure 1**). We present a new fault database for the Tiburon peninsula and use it to generate potential fault geometries for the EPGFZ and nearby faults. We use the observations to develop models of coseismic fault slip and afterslip through four days after the event and compare our results to the seismic-only results of Okuwaki and Fan (2022) and regional topography.

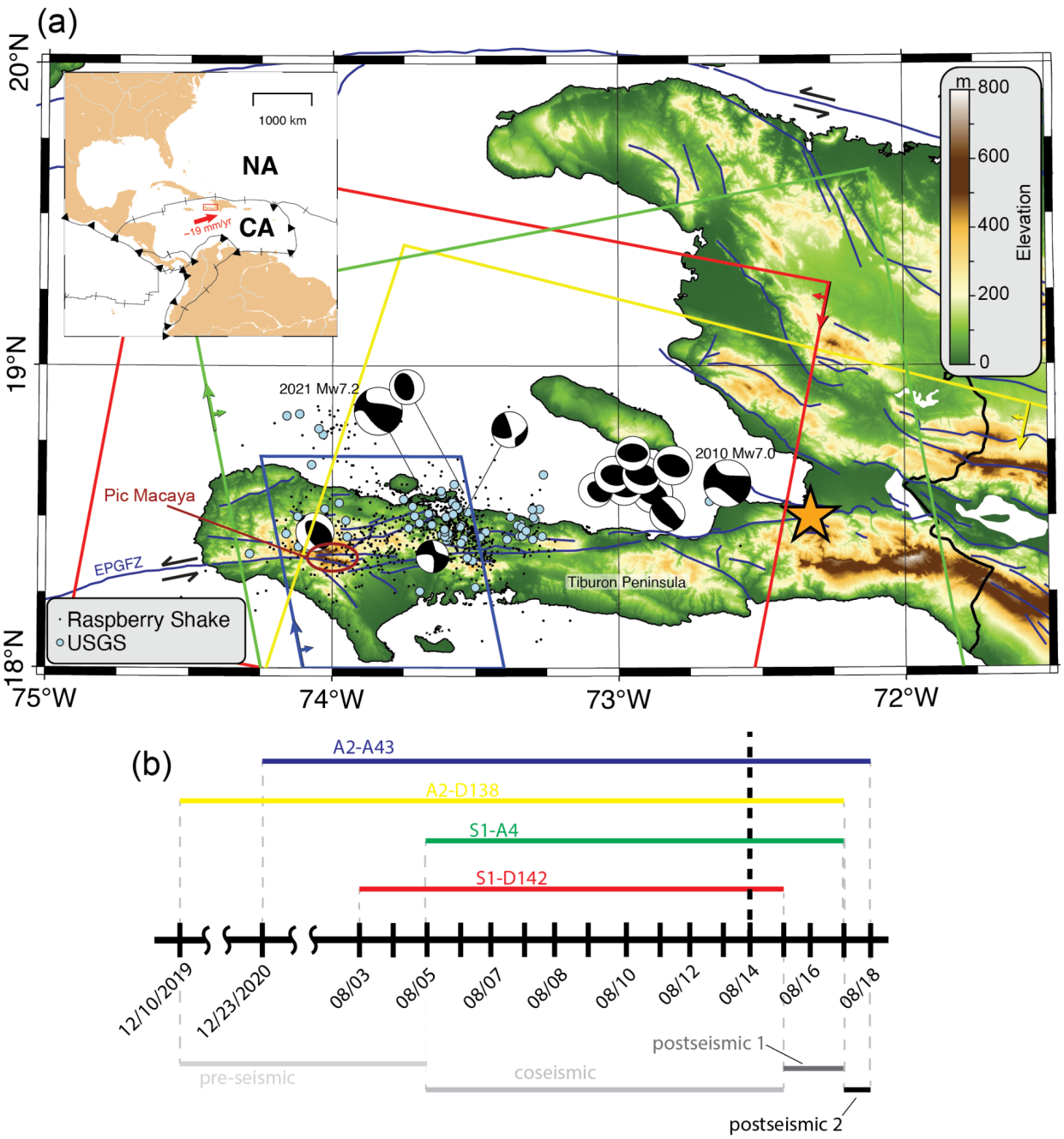

Figure 1. (a) Seismotectonic context and spatial InSAR footprints for the August 2021 Mw 7.2 Haiti earthquake. Thin black lines show the faults from the updated database described in this study. Beachballs are Centroid Moment Tensors (CMTs) for the M_W7.2 mainshock and large aftershocks through January 31, 2022; the location of the 2010 earthquake and large aftershocks are also shown (Dziewonski et al., 1981; Ekström et al., 2012). Gray dots are earthquake locations from COMCAT and black dots are from the Raspberry Shake citizen-seismometer network, both including data from August 13, 2021 - January 31, 2022 (see Data and Resources). Purple lines are the updated CCAF-DB faults. Colored polygons are the outlines of the InSAR tracks used in this study: Sentinel-1 descending track 142 (red), Sentinel-1 ascending track 4 (green), ALOS-2 ascending track 43 (blue), and ALOS-2 descending track 138 (yellow). Orange star is Port-au-Prince. Inset shows the CA plate motion relative to the NA plate. See Data and Resources for details on the digital elevation model and plotting software. **(b)** Temporal footprints of the InSAR observations and corresponding separable slip phases. The time of the earthquake is shown as a vertical

dashed line. The phases given beneath the timeline ("pre-seismic," "coseismic," etc.) represent the different time periods we model separately in the inversion (see Section 2.3).

2 Data and Methods

2.1 Updated fault map database for southern Haiti

We developed a new fault map database through compiling and comparing several sources for fault geometry in Hispaniola (Maurer and Vernon, 2022; **Figure 1**). We complemented the database building on the Caribbean and Central American active fault database (CCAF-DB; Styron et al., 2020). We refined and updated the CCAF-DB by incorporating several additional published sources (Saint Fleur et al., 2020; Possee et al., 2019; Corbeau et al., 2016b; Conrad et al., 2020; French & Schenk, 2004) as well as Shuttle Radar Topography Mission digital elevation model (SRTM) and Light Detection And Ranging (LiDAR) DEMs. We used the updated fault traces database to build a 3D fault model for the earthquake, including southern and northern branches of the EPGFZ, a thrust fault south of the epicentral location, and a larger northern thrust fault (**Figures 1,3** and Supp. Figures S2-S3).

2.2 SAR Observations

We used surface displacements derived from four different SAR ascending and descending tracks (**Figure 2,** Supp. Figure S4-S5). We obtained single-look complex (SLC) SAR images from two Sentinel-1A/B tracks (C-band, ~5.6 cm wavelength), acquired in Terrain Observations with Progressive Scans in azimuth (TOPS) mode. The SLC images were processed with the InSAR Scientific Computing Environment (ISCE) v.2 software (Rosen et al., 2012) "topsApp.py" application. For each track, the secondary radar scenes are geometrically aligned (coregistered) to the reference scene using the Enhanced Spectral Diversity method (ESD; Fattahi et al., 2016). We observed no residual along-track shifts in InSAR with this method. Precise orbit ephemeris data was used to remove orbital contributions from the interferometric phase. We performed regular differential interferometric processing to make interferograms and coherence maps. The interferograms were corrected for topography-related phase components using the 30 m resolution SRTM DEM; (Farr, 2007), filtered using Goldstein-Werner adaptive filtering (Goldstein and Werner, 1998) and unwrapped using the statistical Minimum Cost Flow (MCF) algorithm (Chen and Zebker, 2001; 2002). To produce the SAR pixel offset data, amplitude images were cross-correlated using a matching window of 64 pixels in range and 16 pixels in azimuth. The amplitude images are oversampled by a factor of 64 to obtain 1/64 of a pixel precision. We applied a 500 m median filter to reduce noise. The azimuth offsets were noisy after filtering so we used only the range offsets for modeling.

The ALOS-2 PALSAR-2 L-band (22.9 cm wavelength) interferograms were provided by the Japanese Space Agency (JAXA), and were already fully processed and low-quality pixels masked, so we used these products as provided. We removed disconnected areas away from the main rupture area, especially for descending track (orbit 138). The descending track acquired in ScanSAR mode covered the time period 2019-12-23 to 2021-08-18 (~20 months), while the ascending track (orbit 43) acquired in stripmap mode covered the period 2020-12-23 to 2021-08-17 (~8 months).

Interferograms and dense offset maps were geocoded and downsampled (**Figure 2**). Interferograms were subsampled using a quadtree technique (Jónsson et al., 2002). We used a regular grid with a 3 km median filter to down-sample pixel offsets and further reduce noise. To account for spatially-correlated errors, we estimate variograms and compute full covariance matrices for the observations using data located away from the rupture area (Supp. Figures S6-S7). Some ALOS-2 track 43 displacements show detailed step-overs in fault geometry that are not captured by our model, so we masked out displacements that are on the wrong side of the fault.

We estimate troposphere corrections using the RAiDER package (see Data and Resources). We used the ECMWF ERA-5 weather model (see Data and Resources) to estimate the troposphere total slant delay and corrected the interferograms (e.g. Doin et al., 2009; Jolivet et al., 2014; Bekaert et al., 2015). The correction reduced the RMS phase in Sentinel-1 interferograms but not in ALOS-2 interferograms, so we did not apply the correction for the ALOS-2 data. To account for ionospheric noise, we removed a plane from each InSAR track in the modeling step.

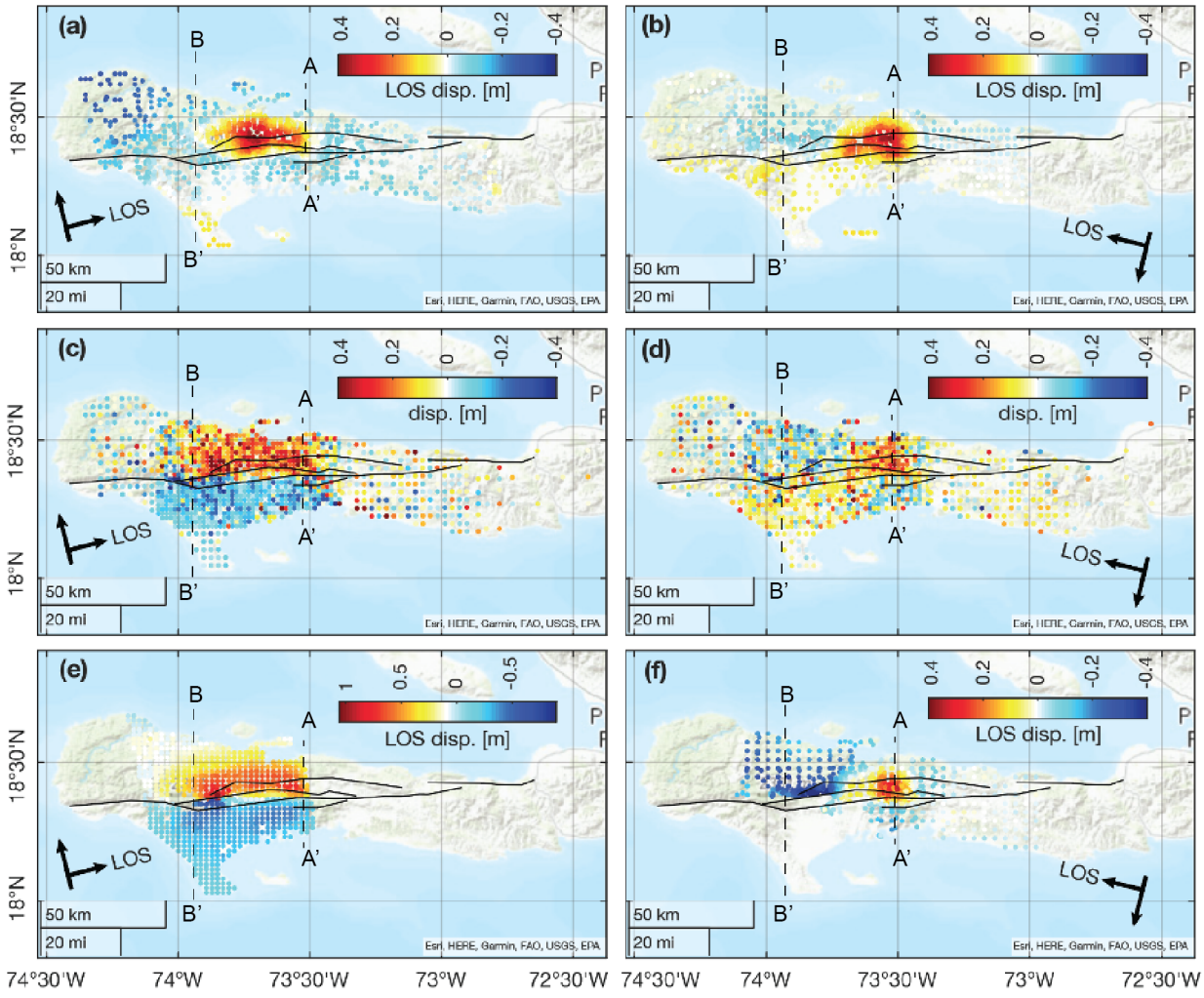

Figure 2. Downsampled InSAR and pixel offset displacements from Sentinel-1 and ALOS-2 used to estimate slip on the fault system. Positive motion is towards the satellite. Top row (a,b) is Sentinel-1 InSAR, middle row (c,d) is Sentinel-1 range pixel offsets, and bottom row (e,f) is ALOS-2 InSAR. Left subpanels (a,c,e) are the ascending data (S1 track 4, A2 track 43) and the right subpanels (b,d,f) are the descending data (S1 track 142, A2 track 138). Data along the profiles A-A' and B-B' are shown in Figure 4.

Visual inspection of the observations show motion towards the satellite (positive) north of the fault just west of 73.5°W in all tracks. Around 74° W the ascending data is positive while descending data show negative displacements impling left-lateral slip. The ascending data in particular shows surface rupture near 74°W (**Figure 2**, Supp. Fig. S4c,e). Taken together, these observations imply that the rupture began as primarily blind reverse-slip in the east and transitioned to primarily left-lateral slip in the west.

2.3 Modeling Approach

The InSAR observations cover different time periods (Supp. Tables S1-S2) meaning that they are sensitive to different phases of displacement. **Figure 1b** shows the different time-periods and which track covers each period. From **Figure 2**, it can be seen that the observations are not all consistent, suggesting that afterslip occurred in the four days following the mainshock. The first SAR acquisition after the earthquake was on August 15th. We refer to all displacements prior to this time as the "coseismic" period, although it may include early postseismic slip up to the acquisition time (about 22 hours after the earthquake). We chose to ignore slip in the pre-seismic time period (i.e., we assume preseismic deformation is zero), because the interseismic slip rate on the EPGFZ is estimated to be ~1cm/yr or less (e.g. Symithe et al., 2015; Symithe & Calais, 2015; 2016; Saint Fleur et al., 2020). Any pre-event displacements are thus likely to be well within the level of misfit for the ALOS-2 tracks (residual 1-sigma of 3.8 cm for D138 and 5.5 cm for A43). We solve for slip during the "coseismic," early postseismic (Aug 15-17) and later postseismic (Aug 17-18) time periods.

We used the updated CCAF database referenced above to construct a "sheets in the wind" fault model for the Tiburon peninsula around the area of the Haiti earthquake. All fault segments were specified to extend from the surface for a width of 24 km and discretized into square patches. We used 10 patches in the down-dip direction, for a patch size of ~2.4 x 2.4 km (Supp. Fig. S3). We generated Green's functions for a uniform elastic half-space using the Okada (1985) algorithm. Supp. Fig.'s S8-S14 show slip and data residuals for several different geometries, including a single fault trace, south-dipping, vertical, and several north-dipping angles. In all models, fault dip on the EPGFZ transitions to vertical in the east (**Figure 3**); this is not required or constrained by the observations but is consistent with prior results for the EPGFZ in that region (e.g. Saint-Fleur et al., 2015; Posse et al., 2018).

We used bounded linear least-squares to solve for slip on the fault using the interior-point algorithm (*lsqlin* in Matlab). Slip is constrained to be left-lateral and reverse-sense with an upper bound of 5 m. We used both minimum-norm and spatial smoothing regularization of the slip solutions, and used an L-curve to determine an appropriate choice for the hyperparameters (Supp. Fig. S15). Representative cases with rougher and smoother slip models are shown in the Supplement (Supp. Figures S16-S17 and Supp. Tables S3-S4). Slip during the second postseismic phase is constrained only by a single interferogram, so we increased the minimum-norm regularization weight for slip in that phase. We conducted a checkerboard test to see how well our datasets resolve slip on the fault in the different time periods (Supp. Figure S18). The test shows that the coseismic and early postseismic phase should be fairly well-resolved over the entire fault system, but not the second postseismic phase, as expected. We do not consider potential contributions to deformation from poroelastic rebound in our modeling.

3 Results

Testing multiple models for fault geometry shows that the InSAR observations require that the EPGFZ itself be dipping to the north in this area. Supplemental Tables S3-S4 show the misfit and total moment associated with alternative geometries. The preferred model, which assumes two sub-parallel strands of the EPGFZ (southern and northern) dipping at 51 degrees to the north, is the most consistent with both the InSAR observations and CMT (reduced χ^2 of 2.1). Fault dip of 40 or 70 degrees to the north fit the observations slightly worse than the preferred model, while both vertical (no reverse slip) and south-dipping fault geometry (allowing reverse

slip) does not fit the observations better (Supp. Table S4-S5). To further verify the fault dip, we conducted a 2D plane-strain inversion and used Markov Chain Monte Carlo (MCMC) sampling to determine a uniform slip and fault dip for a north-south profile across the fault near the hypocenter (see Supplemental Text S2 and Fig. S20). The best-fitting fault dip was 52 degrees, consistent with our 3D experiments.

Fault slip for a representative model is shown in **Figure 3**. During the coseismic phase, and consistent with Okuwaki and Fan (2022), slip occurs in two distinct areas, one of which is located near the hypocenter with peak slip of ~2.7 m at a depth of ~7 km (10 km down-dip), and involves primarily dip-slip faulting on the southern and northern branches of the EPGFZ. The second main area of coseismic slip occurs west of Pic Macaya (**Figure 1**), where our model transitions to a single fault, and involves primarily strike-slip faulting, with peak slip estimated to be 1.2 m at a depth of ~8 km (12 km down-dip). Our results indicate that slip east of Pic Macaya was partitioned between the southern and northern EPGFZ. Shallow left-lateral slip occurred on the southern branch between the reverse-slip rupture center and the restraining bend at Pic Macaya. The rupture extended over 80 km in length on the EPGFZ. The easternmost end of the northern thrust fault in the model has a region of high left-lateral slip during the coseismic phase, which is a consistent feature of all our inversions (see examples in Supp. Fig.'s S9, S17), with peak slip ~1.5 m and a depth of ~7 km. From our geodetic observations alone, we cannot say whether this eastern slip would have been seismic or aseismic or an artifact of using planar fault branches; further detailed analysis including seismic data is required. Predicted 3D displacements from the model in **Figure 3** are shown in Supp. Fig. S19.

Slip during the first postseismic phase (August 15-17) occurs near the edges of coseismic slip areas, and with the same sense of slip. Reverse slip occurs at ~3 km depth just up-dip of the coseismic rupture, with peak slip estimated to be ~1.7 m. Left-lateral slip occurs at the upper-western edge of the mainshock location (~3 km deep, peak slip ~2.2 m), which coincides with the location of a left-lateral M_W4.9 aftershock that occurred on August 15 (**Figure 1a**). About 2.8 m peak left-lateral slip also occurs within the restraining bend. Finally, ~1.2 m left-lateral slip occurs at ~7 km depth on the far western end of the fault. Slip is mostly absent from the other faults in the system during the first postseismic phase. Total moment over the whole fault system during the early postseismic phase is M_W6.8, including the M_W4.9 aftershock.

Slip during the second postseismic phase is not well constrained, due to a single interferogram constraining it (ALOS-2 track 43). We strongly damped slip in the second postseismic phase. However, some slip is required to fit the observations. In particular, slip occurs on the southern and northern EPGFZ near the surface. Total moment during the second

postseismic phase is estimated at ~M_W6.8, but is uncertain due to the strong damping and poor resolution (see Supp. Fig. S18).

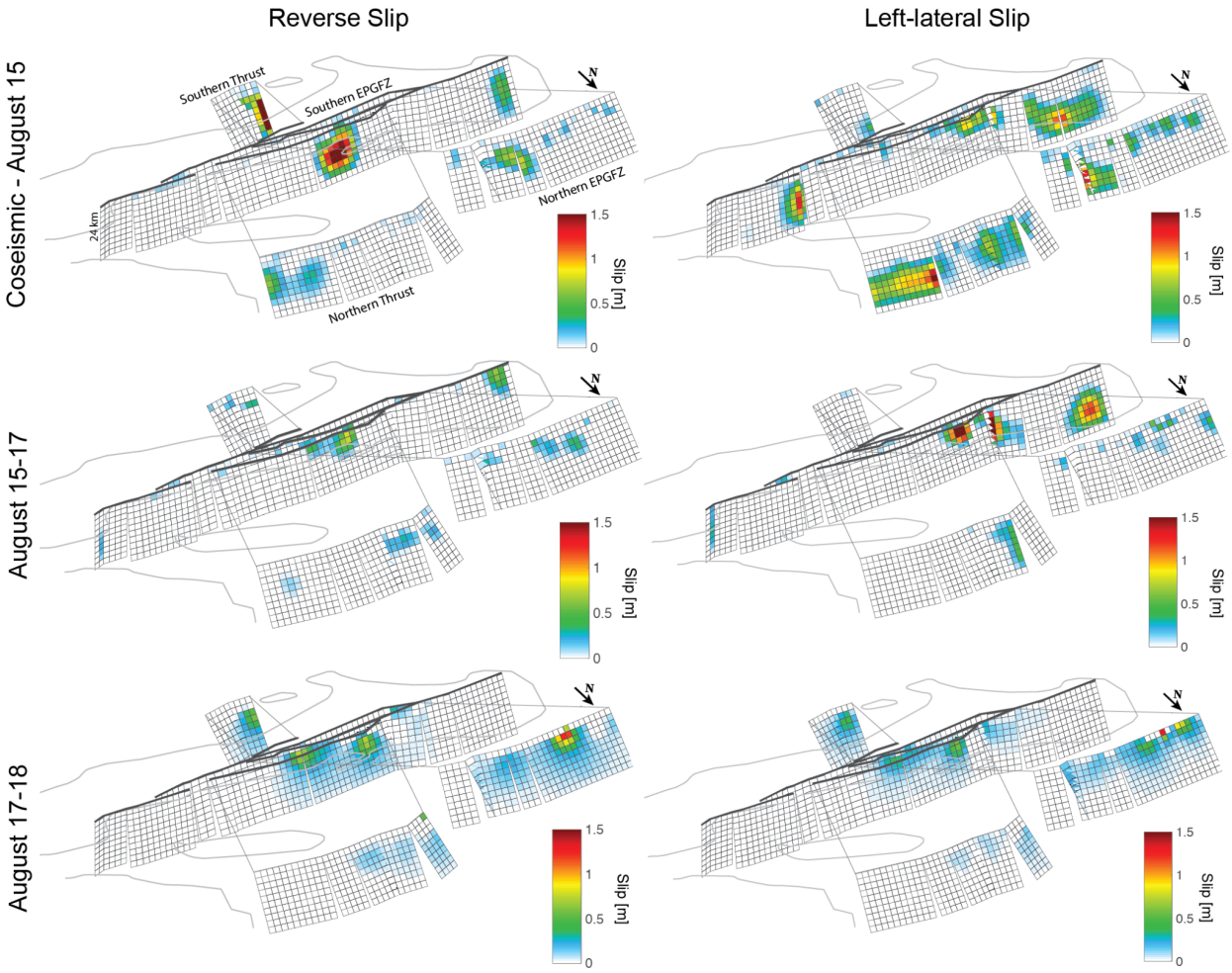

Figure 3. Modeled slip during the different slip phases. The fault system has been exploded and rotated to view from the northeast to aid visualization.

4 Discussion

The preferred model shown in **Figure 3** implies that the 2021 Nippes earthquake activated multiple faults and occurred as two sub-events separated by roughly 60 km. Okuwaki and Fan's (2022) back-projection model is consistent with this picture; they show that their model roughly matched the observed InSAR displacements. Our results are qualitatively consistent with theirs, but in contrast to their study, we find that the data are best explained if both the thrust and left-lateral components of fault slip occurred on the EPGFZ itself. The two sub-events are separated by a restraining bend in the fault at Pic Macaya, which has the highest topography in southwest Haiti. Comparing our results with Okuwaki and Fan's, the rupture

began as primarily a reverse-slip event east of the bend and ruptured west, all but died out in the bend itself (**Figure 3** and Okuwaki and Fan, 2002, their Figures 2 and 3) and then revived west of the bend as a left-lateral rupture; thus, the rupture appears to have "jumped" the restraining bend rather than rupturing through, suggesting that it may have been a dynamically triggered phase of rupture.

The coseismic moment release in all models (including different fault geometries) was lower than the seismically-estimated moment magnitude. This is likely due to a combination of factors. We ignore topography in our modeling, which results in systematically under-estimating the slip (e.g. McTigue and Segall, 1988) in areas of steep topography around the rupture. Lower slip might have been preferred using the minimum-norm regularization. Steeper fault dip used in the other inversion scenarios results in slightly higher moments of 7.1-7.2, albeit with worse fit to the data.

Slip in the second postseismic phase is not well constrained but is required by the observations. Profiles through two areas east of the restraining bend (**Figure 4**) shows that ALOS-2 track 43 has larger displacements than the Sentinel-1 and ALOS-2 track 138 observations, indicating that a phase of late triggered slip occurred on the fault. This late slip, shown in Figure 3 during the second postseismic phase, involved oblique slip only on the EPFGZ east of Pic Macaya. Displacements in Figure 4c also indicate that afterslip reached the surface after the first postseismic phase.

Long-term strike-slip motion on the EGPFZ alone cannot fully explain the high topography in the region. Pic Macaya has the highest topography in southwest Haiti at ~1800 m above sea level and is consistent with push-up tectonics at the restraining bend, while to the east near the hypocenter a broad region of high elevation (750-1050 m) is consist with the location of peak coseismic uplift associated with reverse slip on the EPGFZ (Supp. Fig. S19). Although other nearby faults likely accommodate compressional stresses in the region (e.g. during the 2010 Leogane, Haiti earthquake) the current study suggests that some fraction of regional compression is accommodated by the EPGFZ itself. If this is the case, then long-term slip estimated for left-lateral motion (Saint-Fleur et al., 2020) on the EGPFZ is only a part of the total deformation accommodated by the system.

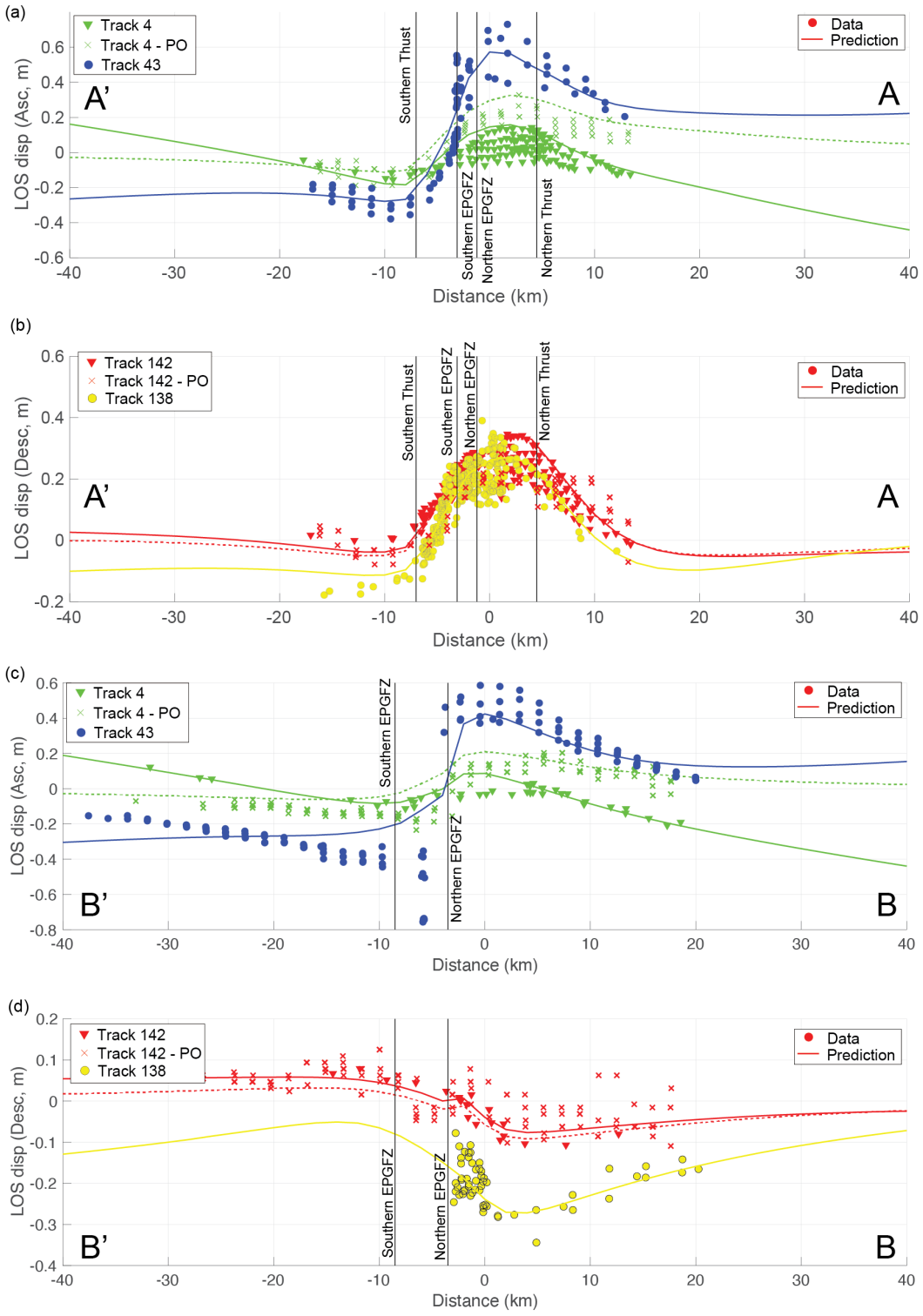

Figure 4. Observed and predicted displacement profiles for the profiles shown in Figure 2. Dashed lines are predicted pixel offsets. (a-b) A-A' profiles; (a) are the ascending tracks and (b)

are the descending tracks. (c-d) B-B' profiles. (c) are the ascending tracks and (d) are the descending tracks.

5 Conclusions

We present a new fault surface trace map of Hispaniola and use it to develop a fault model for the 2021 Nippes, Haiti earthquake. The earthquake ruptured 80 km of the Enriquillo-Plantain Garden Fault Zone (EPGFZ) in two main sub-events separated by ~60 km on either side of a restraining bend at Pic Macaya. About 2.7 m of reverse-slip east of the bend transitions to shallow left-lateral slip on both sides (east and west). Slip jumps the restraining bend at Pic Macaya and ruptured the western EPGFZ with about 1.3 m of left-lateral slip. Estimated coseismic moment magnitude is ~M_W7.1. Afterslip in the four days following the event occurred up-dip and along-strike of the coseismic rupture areas east of Pic Macaya, breaching the surface west of the main reverse faulting area on August 17th or 18th. Afterslip is mainly confined to shallow depths except at the far western end of the EPGFZ. Estimated postseismic moment magnitude is ~M_W7.0.

Acknowledgments

We thank JAXA and the Geospatial Information Authority of Japan for making the ALOS-2 interferograms freely available. We thank ESA for making access to Sentinel-1 data freely available. This work is based in part on data services provided by the OpenTopography Facility with support from the National Science Foundation under NSF Award Numbers 1948997, 1948994 & 1948857. We thank Dr. Jonathan Obrist-Farner and Yi-Chieh Lee for helpful discussions on this topic. The authors have no known conflicts of interest.

Open Research

Data and software for replicating the results presented in this study are archived at Maurer, (2022). We used the UNAVCO plate motion calculator (https://www.unavco.org/software/geodetic-utilities/plate-motion-calculator/plate-motion-calculator.html; last accessed November 24, 2021) to determine the relative motion of the CA plate relative to the NA plate. LiDAR data was retrieved from https://opentopography.org/blog/haiti-lidar-imagery-google-earth, last accessed January 14, 2022. Shuttle Radar Topography Mission (SRTM) 1 Arc-Second Global data was retrieved from https://doi.org/10.5066/F7K072R7, last accessed January 14, 2022.). ALOS-2 interferograms were provided by JAXA and the Geospatial Information Authority in Japan and may be requested from them. Sentinel-1 data were freely provided by the European Space Agency (https://scihub.copernicus.eu/). Centroid moment tensors were obtained from www.globalcmt.org. Some figures were created with PyGMT (https://www.pygmt.org/latest/, Uieda et al., 2021). ISCE2 (https://github.com/isce-framework/isce2) was used for processing interferograms. RAiDER (https://github.com/dbekaert/RAiDER) was used to calculate

tropospheric noise. The ERA-5 data products processed by RAiDER are available from the European Centre for Medium-Range Weather Forecasts (ECMWF) at www.ecmwf.int (last accessed February 1, 2022). The data is published under a Creative Commons Attribution 4.0 International (CC BY 4.0) (see https://creativecommons.org/licenses/by/4.0/). ECMWF does not accept any liability whatsoever for any error or omission in the data, their availability, or for any loss or damage arising from their use.

References

Bakun, W. H., Flores, C. H., & ten Brink, U. S. (2012). Significant Earthquakes on the Enriquillo Fault System, Hispaniola, 1500–2010: Implications for Seismic HazardSignificant Earthquakes on Enriquillo Fault System, Hispaniola, 1500–2010: Implications for Hazard. Bulletin of the Seismological Society of America, 102(1), 18–30. https://doi.org/10.1785/0120110077

Bekaert, D. P. S., Walters, R. J., Wright, T. J., Hooper, A. J., & Parker, D. J. (2015). Statistical comparison of InSAR tropospheric correction techniques. Remote Sensing of Environment, 170, 40–47. https://doi.org/https://doi.org/10.1016/j.rse.2015.08.035

Benford, B., DeMets, C., & Calais, E. (2012). GPS estimates of microplate motions, northern Caribbean: evidence for a Hispaniola microplate and implications for earthquake hazard. Geophysical Journal International, 191(2), 481–490. https://doi.org/10.1111/j.1365-246X.2012.05662.x

Calais, É., Symithe, S., Mercier de Lépinay, B., & Prépetit, C. (2016). Plate boundary segmentation in the northeastern Caribbean from geodetic measurements and Neogene geological observations. Comptes Rendus Geoscience, 348(1), 42–51. https://doi.org/https://doi.org/10.1016/j.crte.2015.10.007

Chen, C. W., & Zebker, H. A. (2001). Two-dimensional phase unwrapping with use of statistical models for cost functions in nonlinear optimization. Journal of the Optical Society of America A, 18(2), 338–351. https://doi.org/10.1364/JOSAA.18.000338

Chen, C. W., & Zebker, H. A. (2002). Phase unwrapping for large SAR interferograms: statistical segmentation and generalized network models. IEEE Transactions on

Geoscience and Remote Sensing, 40(8), 1709–1719. https://doi.org/10.1109/TGRS.2002.802453

Conrad, E. M., Faccenna, C., Stockli, D. F., & Becker, T. (2020, October). Cenozoic evolution of the Northern Caribbean plate boundary: Insights from thermochronomentric, kinematic and geomorphic data. [Poster presentation]. Geological Society of America, USA, 52. https://doi.org/10.1130/abs/2020AM-353996

Corbeau, J., Rolandone, F., Leroy, S., Meyer, B., Mercier de Lépinay, B., Ellouz-Zimmermann, N., & Momplaisir, R. (2016a). How transpressive is the northern Caribbean plate boundary? Tectonics, 35(4), 1032–1046. https://doi.org/10.1002/2015TC003996

Corbeau, J., Rolandone, F., Leroy, S., Mercier de Lépinay, B., Meyer, B., Ellouz-Zimmermann, N., & Momplaisir, R. (2016b). The northern Caribbean plate boundary in the Jamaica Passage: Structure and seismic stratigraphy. Tectonophysics, 675, 209–226. https://doi.org/https://doi.org/10.1016/j.tecto.2016.03.022

DeMets, C., & Wiggins-Grandison, M. (2007). Deformation of Jamaica and motion of the Gonave microplate from GPS and seismic data. *Geophysical Journal International*, *168*(1), 362-378.

DeMets, C., Gordon, R. G., & Argus, D. F. (2010). Geologically current plate motions. Geophysical Journal International, 181(1), 1–80. https://doi.org/10.1111/j.1365-246X.2009.04491.x

Doin, M.-P., Lasserre, C., Peltzer, G., Cavalié, O., & Doubre, C. (2009). Corrections of stratified tropospheric delays in SAR interferometry: Validation with global atmospheric models. Journal of Applied Geophysics, 69(1), 35–50. https://doi.org/https://doi.org/10.1016/j.jappgeo.2009.03.010

Douilly, R., Haase, J. S., Ellsworth, W. L., Bouin, M., Calais, E., Symithe, S. J., Armbruster, J. G., de Lépinay, B. M., Deschamps, A., Mildor, S., Meremonte, M. E., & Hough, S. E. (2013). Crustal Structure and Fault Geometry of the 2010 Haiti Earthquake from Temporary Seismometer Deployments. *Bulletin of the Seismological Society of America*, *103*(4), 2305–2325. https://doi.org/10.1785/0120120303

Douilly, R., H. Aochi, E. Calais, and A. M. Freed (2015), Three-dimensional dynamic rupture simulations across interacting faults: The Mw7.0, 2010, Haiti earthquake, J. Geophys. Res. Solid Earth, 120, doi:10.1002/2014JB011595.

Dziewonski, A. M., T.-A. Chou and J. H. Woodhouse, Determination of earthquake source parameters from waveform data for studies of global and regional seismicity, J. Geophys. Res., 86, 2825-2852, 1981. doi:10.1029/JB086iB04p02825

Ekström, G., M. Nettles, and A. M. Dziewonski, The global CMT project 2004-2010: Centroid-moment tensors for 13,017 earthquakes, Phys. Earth Planet. Inter., 200-201, 1-9, 2012. doi:10.1016/j.pepi.2012.04.002

Farr, T. G., Rosen, P. A., Caro, E., Crippen, R., Duren, R., Hensley, S., Kobrick, M., Paller, M., Rodriguez, E., Roth, L., Seal, D., Shaffer, S., Shimada, J., Umland, J., Werner, M., Oskin, M., Burbank, D., & Alsdorf, D. (2007). The Shuttle Radar Topography Mission. Reviews of Geophysics, 45(2). https://doi.org/https://doi.org/10.1029/2005RG000183

Fattahi, H., Agram, P., & Simons, M. (2017). A Network-Based Enhanced Spectral Diversity Approach for TOPS Time-Series Analysis. IEEE Transactions on Geoscience and Remote Sensing, 55(2), 777–786. https://doi.org/10.1109/TGRS.2016.2614925

French, C. D., & Schenk, C. J., (2004). Map showing geology, oil and gas fields, and geologic provinces of the Caribbean region: U.S. Geological Survey Open-File Report 97-470-K. https://doi.org/10.3133/ofr97470K

Goldstein, R. M., & Werner, C. L. (1998). Radar interferogram filtering for geophysical applications. Geophysical Research Letters, 25(21), 4035–4038. https://doi.org/https://doi.org/10.1029/1998GL900033

Hayes, G. P., Briggs, R. W., Sladen, A., Fielding, E. J., Prentice, C., Hudnut, K., Mann, P., Taylor, F. W., Crone, A. J., Gold, R., Ito, T., & Simons, M. (2010). Complex rupture during the 12 January 2010 Haiti earthquake. Nature Geoscience. https://doi.org/10.1038/ngeo977

Jolivet, R., Grandin, R., Lasserre, C., Doin, M.-P., & Peltzer, G. (2011). Systematic InSAR tropospheric phase delay corrections from global meteorological reanalysis data. Geophysical Research Letters, 38(17), n/a--n/a. https://doi.org/10.1029/2011GL048757

Jónsson, S., Zebker, H., Segall, P., & Amelung, F. (2002). Fault slip distribution of the 1999 M w 7.1 Hector Mine, California, earthquake, estimated from satellite radar and GPS measurements. *Bulletin of the Seismological Society of America*, *92*(4), 1377-1389.

Leroy, S., Ellouz-Zimmermann, N., Corbeau, J., Rolandone, F., de Lepinay, B. M., Meyer, B., ... & Muñoz, S. (2015). Segmentation and kinematics of the North America-Caribbean plate boundary offshore Hispaniola. *Terra Nova*, *27*(6), 467-478.

Lin, Jian, Stein, Ross S., Sevilgen, Volkan, and Toda, Shinji, 2010, USGS-WHOI-DPRI Coulomb stress-transfer model for the January 12, 2010, MW=7.0 Haiti earthquake: U.S. Geological Survey Open-File Report 2010-1019, 7 p.

Manaker, D. M., Calais, E., Freed, A. M., Ali, S. T., Przybylski, P., Mattioli, G., ... & De Chabalier, J. B. (2008). Interseismic plate coupling and strain partitioning in the northeastern Caribbean. *Geophysical Journal International*, *174*(3), 889-903.

Mann, P., Calais, E., Ruegg, J.-C., DeMets, C., Jansma, P. E., & Mattioli, G. S. (2002). Oblique collision in the northeastern Caribbean from GPS measurements and geological observations. Tectonics, 21(6), 7–26. https://doi.org/https://doi.org/10.1029/2001TC001304

Maurer, J. (2022, March 2). 2021 Haiti earthquake. https://doi.org/10.17605/OSF.IO/F8W9E

Maurer, J., & Vernon, A. (2022). CCAF-DB Update (Version 1.0) [Computer software]. https://doi.org/https://doi.org/10.13117/central-america-caribbean-active-faults

McTigue, D. F., & Segall, P. (1988). Displacements and tilts from dip-slip faults and magma chambers beneath irregular surface topography. Geophysical Research Letters, 15(6), 601–604. https://doi.org/https://doi.org/10.1029/GL015i006p00601

Okada, Y. (1985). Surface deformation due to shear and tensile faults in a half-space. Bulletin of the Seismological Society of America, 75(4), 1135–1154.

Okuwaki, R., & Fan, W. (2022). Oblique Convergence Causes Both Thrust and Strike-Slip Ruptures During the 2021 M 7.2 Haiti Earthquake. Geophysical Research Letters, 49(2), e2021GL096373. https://doi.org/https://doi.org/10.1029/2021GL096373

Possee, D., Keir, D., Harmon, N., Rychert, C., Rolandone, F., Leroy, S., Corbeau, J., Stuart, G., Calais, E., Illsley-Kemp, F., Boisson, D., Momplaisir, R., & Prépetit, C. (2019). The Tectonics and Active Faulting of Haiti from Seismicity and Tomography. Tectonics, 38(3), 1138–1155. https://doi.org/10.1029/2018TC005364

Rosen, P. A., Gurrola, E., Sacco, G. F., & Zebker, H. (2012). The InSAR scientific computing environment. *EUSAR 2012; 9th European Conference on Synthetic Aperture Radar*, 730–733.

Saint Fleur, N., Klinger, Y., & Feuillet, N. (2020). Detailed map, displacement, paleoseismology, and segmentation of the Enriquillo-Plantain Garden Fault in Haiti. Tectonophysics, 778, 228368. https://doi.org/https://doi.org/10.1016/j.tecto.2020.228368

Styron, R., García-Pelaez, J., & Pagani, M. (2020). CCAF-DB: the Caribbean and Central American active fault database. Nat. Hazards Earth Syst. Sci., 20(3), 831–857. https://doi.org/10.5194/nhess-20-831-2020

Symithe, S. J., Calais, E., Haase, J. S., Freed, A. M., & Douilly, R. (2013). Coseismic Slip Distribution of the 2010 M 7.0 Haiti Earthquake and Resulting Stress Changes on Regional FaultsCoseismic Slip Distribution of the 2010 M 7.0 Haiti Earthquake. Bulletin of the Seismological Society of America, 103(4), 2326–2343. https://doi.org/10.1785/0120120306

Symithe, S., Calais, E., Chabalier, J. B. De, Robertson, R., & Higgins, M. (2015). Current block motions and strain accumulation on active faults in the Caribbean. Journal of Geophysical Research - Solid Earth, 120(5), 1–27. https://doi.org/10.1002/2014JB011779

Symithe, S., & Calais, E. (2016). Present-day shortening in Southern Haiti from GPS measurements and implications for seismic hazard. *Tectonophysics*, *679*, 117–124. https://doi.org/https://doi.org/10.1016/j.tecto.2016.04.034

Tabrez, A. S., Freed, A. M., Calais, E., Manaker, D. M., & McCann, W. R. (2008). Coulomb stress evolution in Northeastern Caribbean over the past 250 years due to coseismic, postseismic and interseismic deformation. *Geophysical Journal International*, *174*(3), 904-918.

Uieda, L., Tian, D., Leong, W. J., Jones, M., Schlitzer, W., Toney, L., Grund, M., Yao, J., Magen, Y., Materna, K., Newton, T., Anant, A., Ziebarth, M., Wessel, P., & Quinn, J. (2021). PyGMT: A Python interface for the Generic Mapping Tools. https://doi.org/10.5281/ZENODO.5607255

UN Office for the Coordination of Humanitarian Affairs (UN-OCHA). (2021, November 29). Haiti: Earthquake situation report no. 8 - final (29 November 2021). ReliefWeb. Retrieved February 7, 2022, from https://reliefweb.int/report/haiti/haiti-earthquake-situation-report-no-8-final-29-november-2021